Dalton Transactions

Accepted Manuscript

This is an *Accepted Manuscript*, which has been through the Royal Society of Chemistry peer review process and has been accepted for publication.

Accepted Manuscripts are published online shortly after acceptance, before technical editing, formatting and proof reading. Using this free service, authors can make their results available to the community, in citable form, before we publish the edited article. We will replace this *Accepted Manuscript* with the edited and formatted *Advance Article* as soon as it is available.

You can find more information about *Accepted Manuscripts* in the Information for Authors.

Please note that technical editing may introduce minor changes to the text and/or graphics, which may alter content. The journal's standard Terms & Conditions and the Ethical guidelines still apply. In no event shall the Royal Society of Chemistry be held responsible for any errors or omissions in this *Accepted Manuscript* or any consequences arising from the use of any information it contains.

ROYAL SOCIETY OF CHEMISTRY

www.rsc.org/dalton

Dalton Transactions

Dalton Transactions

Dynamic Article Links ►

Cite this: DOI: 10.1039/c0xx00000x

www.rsc.org/xxxxxx

ARTICLE TYPE

Geometric and Electronic Structure of a Peroxomanganese(III) Complex Supported by a Scorpionate Ligand

Hannah E. Colmer, Robert A. Geiger, Domenick F. Leto, Gayan B. Wijeratne, Victor W. Day and Timothy A. Jackson*

Received (in XXX, XXX) Xth XXXXXXXXX 20XX, Accepted Xth XXXXXXXXX 20XX
DOI: 10.1039/b000000x

Abstract. A monomeric Mn^{II} complex has been prepared with the facially-coordinating Tp^{Ph2} ligand, (Tp^{Ph2} = hydrotris(3,5-diphenylpyrazol-1-yl)borate). The X-ray crystal structure shows three coordinating solvent molecules resulting in a six-coordinate complex with Mn-ligand bond lengths that are consistent with a high-spin Mn^{II} ion. Treatment of this Mn^{II} complex with excess KO_2 at room temperature resulted in the formation of a Mn^{III}-O_2 complex that is stable for several days at ambient conditions, allowing for the determination of the X-ray crystal structure of this intermediate. The electronic structure of this peroxomanganese(III) adduct was examined by using electronic absorption, electron paramagnetic resonance (EPR), low-temperature magnetic circular dichroism (MCD), and variable-temperature variable-field (VTVH) MCD spectroscopies. Density functional theory (DFT), time-dependent (TD)-DFT, and multireference *ab initio* CASSCF/NEVPT2 calculations were used to assign the electronic transitions and further investigate the electronic structure of the peroxomanganese(III) species. The lowest ligand-field transition in the electronic absorption spectrum of the Mn^{III}-O_2 complex exhibits a blue shift in energy compared to other previously characterized peroxomanganese(III) complexes that results from a large axial bond elongation, reducing the metal-ligand covalency and stabilizing the σ-antibonding Mn d_{z^2} MO that is the donor MO for this transition.

Introduction

Mononuclear peroxomanganese(III) species have been proposed to form in manganese containing enzymes, including manganese superoxide dismutase (MnSOD),[1-6] manganese-dependent homoprotocatechuate 2,3-dioxygenase (MndD),[7,8] and the oxalate-degrading enzymes oxalate oxidase[9,10] and oxalate decarboxylase.[11-13] These biological peroxomanganese(III) species are highly unstable and relatively little is known concerning their structural and electronic properties. In contrast, a variety of synthetic peroxomanganese(III) species have been generated and characterized, offering insights into the structural, electronic, and reactivity properties of this class of compound.[14-27] Members of this class of compound include side-on peroxomanganese(III) adducts (Mn^{III}-O_2) and end-on alkylperoxomanganese(III) adducts (Mn^{III}-OOR).[28,29]

While there are several examples of Mn^{III}-O_2 complexes with anionic supporting ligands,[14,22,25,30] there are no detailed bonding descriptions of such complexes. As many enzymatic Mn^{III}-O_2 adducts are expected to feature anionic ligands, this represents a gap in knowledge. In addition, the electronic structures of crystallographically characterized Mn^{III}-O_2 adducts have not generally been explored in detail.[30]

A mononuclear Mn^{III}-O_2 complex supported by the monoanionic facially-coordinating trispyrazolyl Tp^{iPr2} ligand (Tp^{iPr2} = hydrotris(3,5-diisopropylpyrazol-1-yl)borate) and an ancillary, monodentate 3,5-isopropylpyrazole ($pz^{iPr2}H$) ligand was previously reported to be stable at room temperature for a few hours.[22] It was observed that the peroxo ligand in this $[Mn^{III}(O_2)(Tp^{iPr2})(pz^{iPr2}H)]$ complex is bound to the Mn^{III} ion in a side-on (η^2) fashion, and the coordination sphere is completed by the four N-donors from the Tp^{iPr2} ligand and the monodentate $pz^{iPr2}H$ ligand. When this Mn^{III}-O_2 complex was cooled from 253 to 193 K, the $pz^{iPr2}H$ ligand formed a hydrogen bond with one O atom of the peroxo unit, and this changed the absorption spectrum.[22,27] Specifically, the absorption maxima shifted from 561 to 583 nm (17 820 to 17 150 cm^{-1}) causing the color of the complex to change from brown (at 253 K) to blue (at 193 K). In contrast, the frequency of the peroxo O-O vibration ($\nu_{O\text{-}O}$), was not perturbed at all by this hydrogen bonding interaction. The absence of a shift in $\nu_{O\text{-}O}$ is surprising, but consistent with the statistically identical O-O bond lengths of the blue and brown isomers (1.43(1) and 1.428(7), respectively).[22] A slightly higher-energy $\nu_{O\text{-}O}$ frequency of 896 cm^{-1} was observed for the related complex $[Mn^{III}(O_2)(Tp)(Me\text{-}Im)]$, which displays an intermolecular hydrogen-bond in the solid-state crystal structure (O-O of 1.42(1) Å).[22]

In a recent review,[23] we noted that Mn^{III}-O_2 adducts supported by the Tp^{iPr2} ligand[22,27] represent a unique geometry compared to other mononuclear Mn^{III}-O_2 adducts. Following a formalism proposed by Kitajima *et al.*,[22] if the peroxo unit is viewed as a monoligand, the τ parameter, as defined in Scheme 1, may be used to classify Mn^{III}-O_2 adducts along a spectrum of geometries from square pyramidal (τ = 0) to trigonal bipyramidal (τ = 1).[23 31] In contrast, crystallographically-characterized mononuclear Mn^{III}-O_2 adducts supported by tetramethylcylam (TMC) and its derivatives (Scheme 1) show τ parameters from 0 to 0.52, with the variation reflecting the size of the macrocyclic ring.[14,21,24]

The Tp-supported Mn^{III}-O_2 adducts also appear distinct from

Dalton Transactions Accepted Manuscript

other mononuclear Mn^{III}-O_2 species in terms of their electronic absorption properties, and this could be related to differences in geometric structure. While the blue and brown isomers of $[Mn^{III}(O_2)(Tp^{iPr2})(pz^{iPr2}H)]$ show only very weak absorption features at ~560 - 580 nm, Mn^{III}-O_2 adducts supported by a variety of neutral N_4 ligands show moderately intense absorption bands from ~415 - 450 nm ($\varepsilon \approx 250 - 500\ M^{-1}cm^{-1}$), with lower-intensity features at ~590 - 620 nm.[23] However, a complication in this comparison is that, while the onset of more intense features at wavelengths lower than 450 nm are apparent in the published electronic absorption spectra of $[Mn^{III}(O_2)(Tp^{iPr2})(pz^{iPr2}H)]$, no absorption maxima were reported.

On the basis of these considerations, we investigated whether a Mn^{III}-O_2 unit could be supported by the related, but synthetically more accessible, Tp^{Ph2} ligand (Scheme 1) in order to more fully understand the spectroscopic properties of a Tp-supported Mn^{III}-O_2 adduct and determine the consequences of the pseudo-trigonal bipyramidal geometry. Herein, we describe the synthesis, structural, and spectroscopic characterization of $[Mn^{III}(O_2)(Tp^{Ph2})(THF)]$, which is formed by treatment of the corresponding Mn^{II} complex with excess KO_2. An X-ray diffraction (XRD) structure of $[Mn^{III}(O_2)(Tp^{Ph2})(THF)]$ reveals a mononuclear Mn^{III}-O_2 unit with the bulky phenyl groups shielding the peroxo ligand.

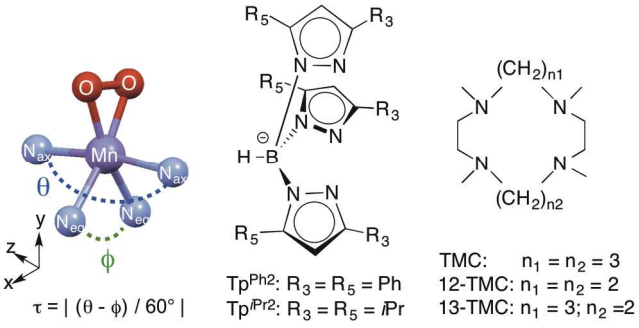

Scheme 1. Representative Mn^{III}-O_2 with calculation of τ (left), Tp type ligands (middle), and TMC type ligands (right).

Electronic absorption, electron paramagnetic resonance (EPR), magnetic circular dichroism (MCD) and variable-temperature, variable-field (VTVH) MCD spectroscopies are used to determine ground-state zero-field splitting parameters and electronic transition energies for this complex. The spin-allowed *d-d* transitions of $[Mn^{III}(O_2)(Tp^{Ph2})(THF)]$, which are highly sensitive to the coordination sphere of the Mn^{III} center, are found to be blue shifted in energy compared to those of other peroxomanganese(III) complexes. The electronic structure causing this perturbation was further investigated using density functional theory (DFT) and multi-reference *ab initio* computations. Previously, spectroscopic changes in some Mn^{III}-O_2 complexes have been attributed to variations in the Mn-O_{peroxo} bond lengths;[16,32] however, as the Mn-O_{peroxo} bond lengths of $[Mn^{III}(O_2)(Tp^{Ph2})(THF)]$ are within the range studied, they cannot account for the large spectroscopic perturbation observed. The combined spectroscopic and computational analysis presented here reveals that, for this system, ligand perturbations perpendicular to the Mn^{III}-O_2 unit can account for spectral differences. This work thus expands upon our previous investigations aiming at defining structural origins of spectral variations in peroxomanganese(III) complexes.[16,18,23,32]

Experimental

Materials

All chemicals and solvents were obtained from commercial vendors at ACS reagent-grade or better and were used without further purification. Synthesis of the Mn^{II} complex was carried out under argon using a glovebox.

Instrumentation

^{1}H NMR spectra were obtained on a Bruker DRX 400 MHz NMR spectrometer. Electronic absorption spectra were recorded on a Cary 50 Bio spectrophotometer (Varian) interfaced with a Unisoku cryostat (USP-203-A). ESI-mass spectrometry experiments were performed using an LCT Primers MicroMass electrospray-ionization time-of-flight instrument. EPR spectra were collected on Bruker EMXPlus instrument with a dual mode cavity. Magnetic circular dichroism (MCD) spectra were collected on a spectropolarimeter (Jasco J-815) interfaced with a magnetocryostat (Oxford Instruments SM-4000-8) capable of horizontal fields up to 8 T.

Preparation of $[Mn^{II}(Tp^{Ph2})(DMF)_3](OTf)$

Potassium tris(3,5-diphenylpyrazol)hydroborate (Tp^{Ph2}) was prepared as previously described by condensing 3 molar equivalents of 3,5-diphenylpyrazole with KBH_4.[33,34] $Mn(OTf)_2$ was prepared by a previously reported procedure by reacting equal molar amounts of $(CH_3)_3Si(OTf)$ and anhydrous $MnCl_2$.[24]

The $[Mn^{II}(Tp^{Ph2})](OTF)$ complex was prepared by adding Tp^{Ph2} (1.0 g, 1.411 mmol) in 30 mL DMF to a stirred solution of $Mn(OTf)_2$ (0.497 g, 1.411 mmol) in 20 mL of DMF. The colorless solution was stirred for 4 hours. Precipitation of the crude product was obtained by addition of diethyl ether. $[Mn^{II}(Tp^{Ph2})(DMF)_3](OTf)$ (1.39 g, 90%) M^+ [({[$Mn(Tp^{Ph2})$]}$^+$) 724.2; requires M^+, 724.2].

In Situ Preparation of $[Mn^{III}(O_2)(Tp^{Ph2})(THF)]$ Complex

The yellow peroxomanganese(III) intermediate was formed by treating a THF solution of $[Mn^{II}(Tp^{Ph2})(DMF)_3](OTf)$ with a KO_2 slurry at ambient conditions. To optimize formation of the peroxomanganese(III) species, the slurry was prepared by stirring 25 equivalents of KO_2 in a 50:50 mixture of 2-Me-tetrahydrofuran:THF for 20 minutes. Treatment with smaller amounts of KO_2 resulted in lower yields of the Mn^{III}-O_2 species. 50 µL of the KO_2 slurry was added to the $[Mn^{II}(Tp^{Ph2})(DMF)_3](OTf)$ solution and stirred for 3 minutes, forming a brown precipitate. A second addition of 50 µL of the KO_2 slurry was added and the solution was stirred for 15 minutes. The brown precipitate was filtered from the solution, and a yellow solution was obtained. The peroxomanganese(III) intermediate was isolated by removing the solvent under vacuum and washing the solid residue with toluene to remove unreacted $[Mn^{II}(Tp^{Ph2})(DMF)_3](OTf)$.

X-ray Crystallography

Single needle crystals of $[Mn^{II}(Tp^{Ph2})(DMF)_3](OTf)$ were grown

Dalton Transactions Accepted Manuscript

This journal is © The Royal Society of Chemistry [year]

by layering heptane on a THF solution of the metal complex at ambient temperature. Single needle crystals of $[Mn^{III}(O_2)(Tp^{Ph2})(THF)]$ were grown by vapor diffusion of diethyl ether into a 50:50 mixture of 2-Me-tetrahydrofuran:THF at -20 °C.

Diffracted intensities were measured for $[Mn^{II}(Tp^{Ph2})(DMF)_3](OTf)$ and $[Mn^{III}(O_2)(Tp^{Ph2})(THF)]$ using monochromated Cu-K_α radiation (λ = 1.54178) on a Bruker Single Crystal Diffraction System equipped with Helios high-brilliance multilayer X-ray optics, an APEX II CCD detector, and a Bruker MicroSTAR microfocus rotating anode X-ray source operated at 45 kV and 60 mA. Lattice constants were determined with the Bruker SAINT software package. The Bruker software package SHELXTL was used to solve the structure using "direct methods" techniques. All states of weighted full-matrix least-squares refinement were conducted using F_o^2 data with the SHELXTL Version 6.10 software package.[35] Crystal data for $[Mn^{II}(Tp^{Ph2})(DMF)_3](OTf)$ and $[Mn^{III}(O_2)(Tp^{Ph2})(THF)]$ are supplied in Table 1, and full data collection and refinement parameters are summarized in the Electronic Supplementary Information (ESI) in Tables S1 and S2.

Table 1. Crystal data for $[Mn(Tp^{Ph2})(DMF)_3](OTf)$ ($C_{59}H_{63}BF_3MnN_9O_7S$) and $[Mn(O_2)(Tp^{Ph2})(THF)]$ ($C_{58}H_{62}BMnN_6O_5$).

formula	$C_{59}H_{63}BF_3MnN_9O_7S$	$C_{58}H_{62}BMnN_6O_5$
MW	1164.99	988.89
T, K	100(2)	100(2)
unit cell	monoclinic	monoclinic
a, Å	17.6441(10)	12.928(2)
b, Å	14.8052(8)	21.642(4)
c, Å	21.9441(11)	18.633(3)
□	90	90
□	93.243(4)	103.572(4)
□	90	90
V, Å^3	5723.2(5)	5067.5(15)
Z	4	4
d(calcd), g/cm^3	1.352	1.296
space group	P2(1)/n	P2(1)/n
R	0.0638	0.0514
R_w	0.1649	0.1474
GOF	0.928	1.077

$$R = \Sigma \, ||F_o| - |F_c|| \, / \, \Sigma \, |F_o|$$

$$R_w = \{ \Sigma \, [w(F_o^2 - F_c^2)^2] \, / \, \Sigma \, [w(F_o^2)^2] \}^{1/2}$$

EPR Experiments

A frozen sample of $[Mn^{II}(Tp^{Ph2})(DMF)_3](OTf)$ (250 µm) was prepared in THF at ambient temperature and flash-frozen in a quartz EPR tube in liquid N_2. Collection of EPR data in the same solvent as MCD experiments (75:25 mixture of 2-Me-tetrahydrofuran:THF, *vide infra*) was unsuccessful due to the propensity of this solvent system to partially melt during transfer of the EPR tubes from the liquid nitrogen storage dewar to the EPR cryostat, resulting in shattered EPR tubes. An EPR sample of $[Mn^{III}(O_2)(Tp^{Ph2})(THF)]$ was prepared after filtering the brown precipitate from the yellow solution and confirming the characteristic spectrum of this complex by UV-visible spectroscopy. Frozen samples of $[Mn^{III}(O_2)(Tp^{Ph2})(THF)]$ (250 µm), prepared using both the crude yellow residue and the purified residue obtained through a toluene wash, were prepared in THF at ambient temperature and flash-frozen in quartz EPR tubes in liquid N_2. All data were collected on an X-band (9 GHz) Bruker EMXPlus spectrophotometer with an Oxford ESR900 continuous-flow liquid helium cryostat and an Oxford ITC503 temperature system to regulate the temperature. To collect perpendicular and parallel-mode spectra, a Bruker ER4116DM dual-mode cavity was used. Spectra were collected under non-saturated conditions with 9.3918 GHz microwave frequency, 20 dB microwave power, 0.6 mT modulation amplitude, 100 kHz modulation frequency and 163 ms time constant. The Matlab-based EPR simulation software package *EasySpin,* developed by Stoll,[36] was used to simulate and fit all EPR spectra and to determine zero-field splitting parameters of the peroxomanganese(III) complex.

Magnetic Circular Dichroism Experiments

A frozen glass sample of $[Mn^{III}(O_2)(Tp^{Ph2})(THF)]$ (15 mM) was prepared in 75:25 mixture of 2-Me-tetrahydrofuran:THF at ambient temperature, transferred to MCD cells, and flash-frozen in liquid N_2. The obtained MCD spectra were measured in mdeg (θ) and converted to Δε ($M^{-1}cm^{-1}$) using the standard conversion factor $\Delta\varepsilon = \theta/(32980 \cdot c \cdot d)$, where *c* is the concentration of the sample and *d* is the path length. MCD spectra were collected at 2, 4, 8, and 15 K for positive and negative field strengths of 1 to 7 T in 1 T increments. VTVH data were fit using the general method developed by Neese and Solomon.[37] Fits were performed for an *S* = 2 system with isotropic *g*-values of 2.00. Using a previously described protocol,[3] zero-field splitting (ZFS) parameters *D* and *E/D* were systematically varied while the transition moment products were optimized for a given set of ZFS parameters. The goodness of fit was evaluated by the χ^2 factor; where χ^2 is the sum of the squares of the differences between experimental and fit data sets.

X-ray Absorption Spectroscopy

The $[Mn^{II}(Tp^{Ph2})(DMF)_3](OTf)$ XAS sample was prepared as a 4% (w/w) dispersion by grinding 8 mg of $[Mn^{II}(Tp^{Ph2})(DMF)_3](OTf)$ with 192 mg boron nitride into a powder with a mortar and pestle. Solution phase XAS samples of $[Mn^{III}(O_2)(Tp^{Ph2})(THF)]$ were prepared by several methods and then transferred to XAS sample holders and flash frozen in liquid N_2. Methods of solution preparation included: 15 mM $[Mn^{III}(O_2)(Tp^{Ph2})(THF)]$ in 50:50 2-Me-tetrahydrofuran:THF, 5 mM $[Mn^{III}(O_2)(Tp^{Ph2})(THF)]$ in THF, and 15 mM $[Mn^{III}(O_2)(Tp^{Ph2})(THF)]$ in THF with isolation by toluene wash. All attempts at XAS data collection for $[Mn^{III}(O_2)(Tp^{Ph2})(THF)]$ were thwarted by photoreduction or sample degradation. XAS spectra were recorded on beamline X3B at the National Synchrotron Light Source (NSLS), Brookhaven National Lab (storage ring conditions, 2.8 GeV, 100 - 300 mA). Mn K-edge X-ray absorption spectra over the energy range 6.4 – 7.4 keV (Si(111) monochrometer) were recorded on a powder sample maintained at 20 K with a helium Displex closed-cycle cryostat. XAS spectra were obtained as fluorescence excitation spectra using a solid-state 13-element germanium detector (Canberra). Contamination of higher harmonics radiation was minimized with a harmonic rejection mirror. Background fluorescence signal was

Dalton Transactions Accepted Manuscript

reduced with a 3 μm chromium filter. A manganese foil spectrum was recorded concomitantly for internal energy calibration, and the first inflection point of the K-edge energy was assigned to 6539.0 eV. Spectra were measured with 5 eV steps below the edge (6359 – 6529 eV), 0.3 eV steps in the edge region (6529 – 6564 eV), and steps equivalent to 0.05 $Å^{-1}$ increments above the edge.

EXAFS data reduction and averaging were performed using the program EXAFSPAK.[38] The pre-edge background intensity was removed by fitting a Gaussian function to the pre-edge background and then subtracting this function from the whole spectrum. The spectrum was also fit with a three-segment spline with fourth-order polynomial components to remove low-frequency background. EXAFS refinement was carried out on $k^3\chi(k)$ data, using phase and amplitude functions obtained from *FEFF*, version 6,[39] and a structural model of $[Mn^{II}(Tp^{Ph2})(DMF)_3](OTf)$ with XRD coordinates. For each fit, the parameters r (average distance between Mn and scattering atom) and σ^2 (Debye-Waller factor) were optimized, while n, the number of atoms in the shell, was kept fixed. n was varied by integer steps systematically. The goodness-of-fit (GOF) was evaluated by the parameter F, where $F = \Sigma\ (\chi_{calcd} - \chi_{expt})^2 / N$, and N is the number of data points. The threshold energy, E_0, in electronvolts (k = 0 point) was kept at a common, variable value for every shell of a given fit.

Density Functional Theory Calculations

The *ORCA* 3.0.1 software package was used for all DFT computations.[40] An initial model of $[Mn^{III}(O_2)(Tp^{Ph2})(THF)]$ was built using the X-ray coordinates obtained in this work. Models of the brown and blue isomers of $[Mn^{III}(O_2)(Tp^{iPr2})(pz^{iPr2}H)]$ were built using the X-ray coordinates of these complexes.[22] Geometry optimizations of these models were converged to the S = 2 spin state. These calculations employed the Becke-Perdew (BP86) functional[41,42] and the SVP (Ahlrichs split valence polarized)[43,44] basis sets with the SV/J auxiliary basis sets for all atoms except for manganese, nitrogen, and oxygen, where the larger TZVP (Ahlrichs triple-ζ valence polarized)[20] basis sets in conjunction with the TZV/J auxiliary basis sets were used. The resolution of identity (RI) approximation[45] was used for all calculations. Solvation effects associated with THF (dielectric constant ε = 7.25) for the Tp^{Ph2} complexes and toluene (dielectric constant ε = 2.40) for the Tp^{iPr2} complexes were incorporated using COSMO, as implemented in *ORCA*.[46] Cartesian coordinates for all DFT-optimized models are included in ESI (Tables S3-S8).

Electronic transition energies and intensities were computed for $[Mn^{III}(O_2)(Tp^{Ph2})(THF)]$ and the brown and blue isomers of $[Mn^{III}(O_2)(Tp^{iPr2})(pz^{iPr2}H)]$ using the TD-DFT method[47-49] within the Tamm-Dancoff approximation.[50,51] These calculations employed the B3LYP functional,[52-54] and the SVP basis set for all atoms except for manganese, nitrogen, and oxygen, where the larger TZVP was used. For the $[Mn^{III}(O_2)(Tp^{Ph2})(THF)]$ calculation, 40 excited states were calculated by including all one-electron excitations within an energy window of ±3 Hartrees with respect to the HOMO/LUMO energies. Additionally, truncated versions of $[Mn^{III}(O_2)(Tp^{Ph2})(THF)]$ were also employed for TD-DFT calculations, however, the full molecule yielded the optimal results. For the larger $[Mn^{III}(O_2)(Tp^{iPr2})(pz^{iPr2}H)]$ complexes, 20 excited states were calculated using the full complex. Isosurface plots of molecular orbitals (MOs) and electron density difference maps (EDDMs) were generated using the gOpenMol program using isodensity values of 0.01 and 0.005 b^{-3}, respectively. Additional electronic transition calculations were performed for $[Mn^{III}(O_2)(Tp^{Ph2})(THF)]$ using the CASSCF calculations in conjunction with second-order-*N*-electron valence state perturbation theory (NEVPT2) method.[55] These calculations employed the RI approximation[45] and the TZVP basis set for manganese, nitrogen, and oxygen and SVP for all other atoms. The active space was selected to include CAS(4, 5), which includes all the 3*d* electrons of the Mn^{III} center, and was calculated with five quintet roots and ten triplet roots.

Results and Discussion

Structural properties of $[Mn^{II}(Tp^{Ph2})(DMF)_3](OTf)$

The Mn^{II} complex $[Mn^{II}(Tp^{Ph2})(DMF)_3](OTf)$ was generated by treatment of $Mn(OTf)_2$ with Tp^{Ph2} in dimethylformamide (DMF). Diffraction quality crystals were obtained by vapour diffusion of diethyl ether into the DMF solution of $[Mn^{II}(Tp^{Ph2})(DMF)_3](OTf)$. Figure 1 (left) displays an ORTEP diagram for $[Mn^{II}(Tp^{Ph2})(DMF)_3](OTf)$. Selected bond distances and angles are given in Table 2. The tridentate Tp^{Ph2} ligand is bound facially, creating three coordination sites occupied by DMF ligands that complete the coordination sphere to give a six-coordinate Mn^{II} ion in a distorted octahedral geometry. The Mn-ligand bond lengths range from ~2.14 to 2.32 Å, typical of a high-spin Mn^{II} ion, and also consistent with reports of previously characterized Mn^{II} species supported by Tp-based ligands.[56-58] Specifically, the Mn-$N_{pyrazole}$ bond lengths of $[Mn^{II}(Tp^{Ph2})(DMF)_3](OTf)$ and other mononuclear Mn^{II} complexes fall within the range of 2.149(2) to 2.319(1) Å (Table 3). Figure 1 (right) displays a view along the three-fold axis of the space filling model for $[Mn^{II}(Tp^{Ph2})(DMF)_3](OTf)$ without the coordinated solvent molecules. This perspective highlights the

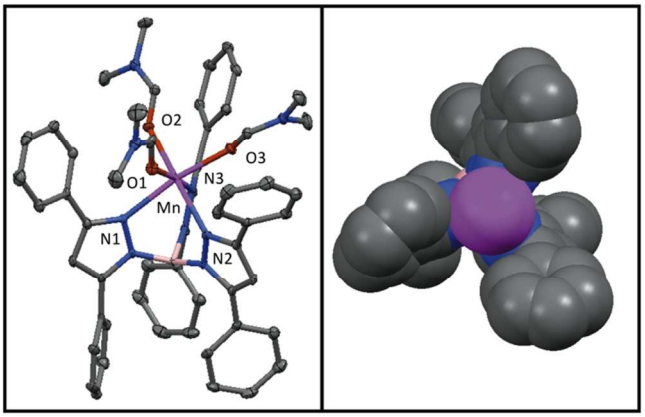

Figure 1. ORTEP diagram of $[Mn^{II}(Tp^{Ph2})(DMF)_3](OTf)$ (left) and space filling model (right). For the ORTEP diagram, hydrogen atoms and the counter anion have been removed for clarity. For the space filling model hydrogen atoms, coordinating solvents molecules, and the counter anion have been removed for clarity. The significant interatomic distances and angles are listed in Table 2.

Dalton Transactions Accepted Manuscript

This journal is © The Royal Society of Chemistry [year]

Table 2. Selected bond lengths (Å) and angles (°) for $[Mn^{II}(Tp^{Ph2})(DMF)_3](OTf)$.

Mn-N(1)	2.286(1)	N(1)-Mn-O(3)	169.1(5)
Mn-N(2)	2.250(3)	N(2)-Mn-O(2)	172.0(2)
Mn-N(3)	2.319(1)	N(3)-Mn-O(1)	171.6(2)
Mn-O(1)	2.157(3)	N(1)-Mn-N(2)	83.3(4)
Mn-O(2)	2.141(6)	N(1)-Mn-N(3)	86.5(2)
Mn-O(3)	2.191(1)	N(2)-Mn-N(3)	86.7(9)

Table 3. Mn-$N_{pyrazole}$ bond lengths (Å) for $[Mn^{II}(Tp^{Ph2})(DMF)_3](OTf)$ and other $Mn^{II}(Tp)$ complexes.

	Mn-N(1)	Mn-N(2)	Mn-N(3)	Ref
$[Mn^{II}(Tp^{Ph2})(DMF)_3](OTf)$	2.286(1)	2.250(3)	2.319(1)	This work
$[Mn(Tp^{CO2Et,Me})(H_2O)_3]ClO_4$	2.254(4)	2.273(4)	2.307(4)	56
$[Mn(OAc)(Tp^{Ph,Me})(pz^{Ph,Me}H)]$	2.199(2)	2.282(2)	2.149(2)	57
$[Mn(Cl)(Tp^{iPr2})(pz^{iPr2}H)]$	2.151(2)	2.164(2)	2.243(2)	57

open face of the metal ion that is shielded by the phenyl groups of the supporting ligand.

Conversion of $[Mn^{II}(Tp^{Ph2})(DMF)_3](OTf)$ to $[Mn^{III}(O_2)(Tp^{Ph2})(THF)]$

No intense features are observed in the electronic absorption spectra of tetrahydrofuran (THF) solutions of $[Mn^{II}(Tp^{Ph2})(DMF)_3](OTf)$ at energies below 33 000 cm^{-1} (Figure 2; dashed line). A weak feature is observed at ~28 000 cm^{-1} (ε = 20 $M^{-1}cm^{-1}$) that could arise from a Mn^{II}-to-ligand (Tp^{Ph2}) charge-transfer (CT) transition. While the intensity is very low for a CT feature, the intensity of this band is at least an order of magnitude larger than that expected for a spin-forbidden Mn^{II} ligand-field transition.[59]

Treatment of $[Mn^{II}(Tp^{Ph2})(DMF)_3](OTf)$ with excess KO_2 at room temperature results in the formation of a yellow intermediate and a brown precipitate. After filtering the brown precipitate from the solution to obtain the yellow intermediate, new absorption features are present in the visible region. The absorption spectra of the yellow intermediate is characterized by a prominent band at 26 385 cm^{-1} and a weaker, broader band at 22 936 cm^{-1} (ε = 324 and 73 M^{-1} cm^{-1}, respectively). For the previously reported $[Mn^{III}(O_2)(Tp^{iPr2})(pz^{iPr2}H)]$ complex, a weak, broad band was observed at 17 800 cm^{-1} which shifted to 17 150 cm^{-1} when a pyrazole-peroxo hydrogen bond was formed.[22] More intense features were apparent at higher energy, but no band maxima were reported. The extinction coefficient for the ~17 000 cm^{-1} transition of $[Mn^{III}(O_2)(Tp^{iPr2})(pz^{iPr2}H)]$ (~50 M^{-1} cm^{-1}) is similar to that of the lowest-energy band of the yellow intermediate. Thus, these data are supportive of the formulation of the yellow intermediate as a peroxomanganese(III) adduct. Unlike the low-energy absorption band of the $[Mn^{III}(O_2)(Tp^{iPr2})(pz^{iPr2}H)]$ complex that red-shifts and increases in intensity upon cooling from 253 to 193 K,[14] the absorption bands of the yellow intermediate sharpen and show a slight blue-shift (~100 cm^{-1}) and increase in intensity (~17 % for the intense band at 26 320 cm^{-1}) when a 75:25 mixture of 2-Me-tetrahydrofuran:THF solution of the sample is cooled from 300 to 200 K (ESI Figure S1).

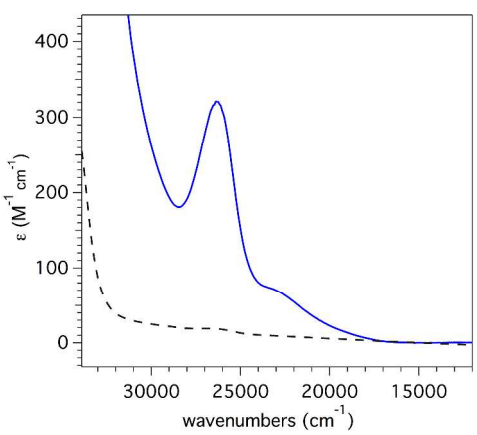

Figure 2. Electronic absorption spectra of $[Mn^{II}(Tp^{Ph2})(DMF)_3](OTf)$ (black dashed trace) and the yellow intermediate, $[Mn^{III}(O_2)(Tp^{Ph2})(THF)]$, (solid blue trace) at 298 K in THF.

X-ray Diffraction Structure of the yellow intermediate: $[Mn^{III}(O_2)(Tp^{Ph2})(THF)]$

Because of the high thermal stability of the yellow intermediate ($t_{1/2}$ = 4.5 days in THF), we were able to obtain single crystals suitable for XRD experiments. The XRD structure of the yellow needle crystals revealed a neutral mononuclear six-coordinate Mn^{III} complex with a side-on peroxo ligand and a coordinated THF molecule, $[Mn^{III}(O_2)(Tp^{Ph2})(THF)]$ (Figure 3). Selected bond distances and angles are given the Table 4. The Mn^{III} ion is in a distorted octahedral geometry with an axial elongation along the (THF)O-Mn-N(1) axis (bond lengths of 2.313(7) Å and 2.375(2) Å, respectively). Here, the peroxo ligand and the N2 and N3 atoms of the Tp^{Ph} ligand define the equatorial plane. The other Mn-N bond distances are nearly identical, with Mn-N(2) and Mn-N(3) bond lengths of 2.09 Å. The peroxo ligand is nearly symmetrically bound to the Mn^{III} ion with Mn-O distances of 1.865(2) and 1.859(2). The O-O bond length is 1.432(3) Å, which is typical of a peroxo ligand bound to a transition-metal ion and is in good agreement with other reported Mn^{III}-O_2 complexes (Table 2).[22,27,14,24,30] Considering the peroxo as a monoligand, a τ parameter of 1.2 is obtained, indicating that this complex is at the

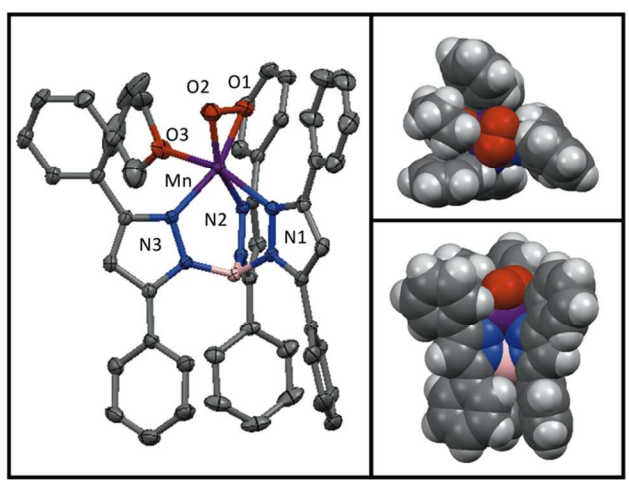

Figure 3. ORTEP diagram of $[Mn^{III}(O_2)(Tp^{Ph2})(THF)]$ (left) and space filling models (right). For the ORTEP diagram, hydrogen atoms have been removed for clarity. Select interatomic distances and angles are listed in Table 4.

Dalton Transactions Accepted Manuscript

Table 4. Selected bond lengths (Å) and angles (°) for[$Mn^{III}(O_2)(Tp^{Ph2})$(THF)].

Mn-O(1)	1.865(2)	O(1)-O(2)	1.432(3)
Mn-O(2)	1.859(2)	N(2)-Mn-O(1)	109.1(2)
Mn-O(3)[a]	2.313(7)	N(3)-Mn-O(2)	111.9(9)
Mn-N(1)	2.375(2)	N(1)-Mn-O(3)[a]	163.1(2)
Mn-N(2)	2.095(2)	N(1)-Mn-N(3)	84.5(1)
Mn-N(3)	2.091(2)	N(1)-Mn-N(2)	84.6(9)

[a]O(3) refers to the O atom of the THF ligand

trigonal bipyramidal limit, similar to other Tp-supported Mn^{III}-O_2 adducts.[23] (The τ parameter of greater than 1, which would not be possible for authentic five-coordinate complexes, results from our specific definition of τ for Mn^{III}-O_2 adducts.[31]) Figure 3 (right) displays perpendicular views of the space filling model for [$Mn^{III}(O)_2(Tp^{Ph2})$(THF)]. The peroxo ligand is well shielded by the three phenyl groups of the Tp^{Ph2} ligand, which could account for the high thermal stability of this complex.

EPR Experiments

X-band EPR spectra were collected for frozen solutions of [$Mn^{II}(Tp^{Ph2})(DMF)_3$](OTf) and [$Mn^{III}(O_2)(Tp^{Ph2})$(THF)] at 5 K in perpendicular and parallel mode. In perpendicular mode, a THF solution of [$Mn^{II}(Tp^{Ph2})(DMF)_3$](OTf) exhibits a 6-line signal at g_1 = 2.03 with hyperfine splitting of 9.1 mT, indicative of mononuclear Mn^{II} (Figure 4, left; black trace). Additionally, a weaker feature at g_2 = 4.1 is present with hyperfine splitting of 7.9 mT. Upon the treatment of this solution with an excess of KO_2 and filtering to remove the brown precipitate, a 93% decrease in the intensity at g_1 is observed. (Figure 4, left; blue trace). No signals are observed in the parallel-mode spectrum of this crude solution. Isolation of [$Mn^{III}(O_2)(Tp^{Ph2})$(THF)] by removing the solvent under vacuum and washing with toluene further decreased the intensity at g_1 by a total of 98% (Figure 4, left; red trace). A parallel mode spectrum of this purified sample of the yellow intermediate exhibits a characteristic Mn^{III} feature at g = 8.3 with hyperfine splitting of 5.06 mT (Figure 4, right). Variable-temperature parallel-mode spectra collected from 5 to 20 K revealed an inverse temperature dependence, indicating a negative sign of the axial zero-field splitting (ZFS) parameter D (ESI, Figure S2). The EPR data for [$Mn^{III}(O_2)(Tp^{Ph2})$(THF)] were simulated with g = 1.98, S = 2, a hyperfine splitting of 5.1 mT and the ZFS parameters D = 2.0(5) cm^{-1} and E/D = 0.07(1). (Figure 4, right). The goodness of fit of the simulation was extremely sensitive to changes in the magnitude of E/D (varied in increments of 0.01 cm^{-1}) and less sensitive to the magnitude of D (varied in increments of 0.1 cm^{-1}). The sensitivity of these parameters arises because the value of E determines the splitting of the m_s ± 2 levels that gives rise to the EPR signal, and a value of D that is greater than the microwave quantum value does not significantly impact the EPR signal.

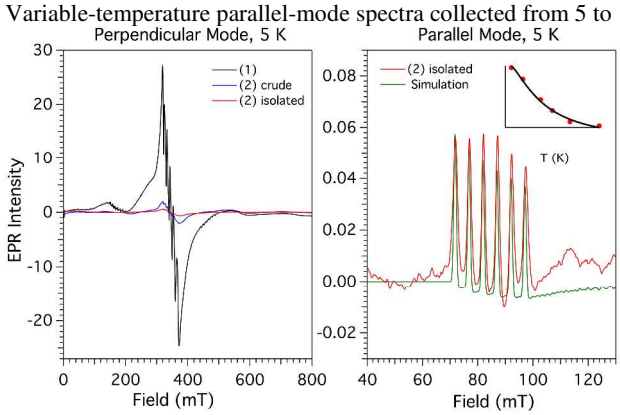

Figure 4. Left: 5 K perpendicular-mode EPR spectrum of the conversion of [$Mn^{II}(Tp^{Ph2})(DMF)_3$](OTf) to [$Mn^{III}(O_2)(Tp^{Ph2})$(THF)] and purification of [$Mn^{III}(O_2)(Tp^{Ph2})$(THF)]. Right: 5 K parallel-mode EPR spectrum of [$Mn^{III}(O_2)(Tp^{Ph2})$(THF)] (red) and simulation (green) with D = -2.0(5), E/D = 0.07(1). Inset: signal intensity versus temperature of g = 8.3 signal. An EPR spectrum of [$Mn^{III}(O_2)(Tp^{Ph2})$(THF)] showing a wider field is in ESI, Figure S3.

Further Spectroscopic Characterization of [$Mn^{III}(O_2)(Tp^{Ph2})$(THF)]

IR data collected for a KBr pellet of [$Mn^{III}(O_2)(Tp^{Ph2})$(THF)] show a weak feature at 882 cm^{-1} (ESI, Figure S4) which is in the expected region for an O-O vibration of a mononuclear Mn^{III}-O_2 adduct (ν_{O-O} = 875 – 896 cm^{-1}).[23] Because solid samples of [$Mn^{III}(O_2)(Tp^{Ph2})$(THF)] could only be successfully prepared using a large excess of KO_2, and we were unable to collect reliable IR data for solution samples of [$Mn^{III}(O_2)(Tp^{Ph2})$(THF)], we did not attempt any isotopic labelling studies using $K^{18}O_2$. Although the peak at 882 cm^{-1} is not observed in the corresponding IR spectrum of [$Mn^{II}(Tp^{Ph2})(DMF)_3$](OTf), (Figure S4), we cannot definitively assign the band at 882 cm^{-1} as the ν_{O-O} mode of [$Mn^{III}(O_2)(Tp^{Ph2})$(THF)] in the absence of the isotopic labelling experiment.

To gain additional insights into the ground- and excited-state properties of [$Mn^{III}(O_2)(Tp^{Ph2})$(THF)], we collected low-temperature MCD and VTVH MCD data. All MCD signals of [$Mn^{III}(O_2)(Tp^{Ph2})$(THF)] observed from 15 000 to 32 000 cm^{-1} show C-term behavior (*i.e.*, their intensities show an inverse temperature dependence; see ESI Figure S5). Figure 5 (bottom) shows the 2 K, 7 T MCD spectra of [$Mn^{III}(O_2)(Tp^{Ph2})$(THF)]. The corresponding 298 K electronic absorption spectrum is included for comparison (Figure 5, top). In the absorption spectrum, [$Mn^{III}(O_2)(Tp^{Ph2})$(THF)] shows low-intensity features from ~18 000 – 24 000 cm^{-1} with a slight maximum at 22 900 cm^{-1}. This fairly indistinct region of the absorption spectrum corresponds to a set of MCD features at 19 000 (-), 22 200 (+), 23 500 (-, shoulder), and 24 100 (-) cm^{-1}. The major absorption band at 26 320 cm^{-1} corresponds to an intense, positively-signed MCD band at roughly the same energy (26 200 cm^{-1}). An iterative Gaussian deconvolution of the absorption and MCD spectra reveals a total of nine electronic transitions from 16 500 to 31 000 cm^{-1} (ESI, Table S9). Tentative assignments can be made for these transitions on the basis of the different selection rules for electronic absorption and MCD spectroscopy, as well as previous spectral analysis of mononuclear Mn^{III}-O_2 adducts.[16] More detailed band assignments developed using TD-DFT computations are discussed later. Bands 2, 8, and 9, which are fairly prominent in the absorption spectrum but carry comparatively little MCD intensity are assigned as peroxo-to-manganese(III) CT transitions (Table 5).[60] Bands 4 and 6, which exhibit very narrow bandwidths in the MCD spectrum and carry

Dalton Transactions Accepted Manuscript

This journal is © The Royal Society of Chemistry [year]

essentially negligible absorption intensity, are assigned as spin-forbidden Mn^{III} *d-d* transitions (Table 5). The narrow widths of these transitions are indicative of small excited state distortions

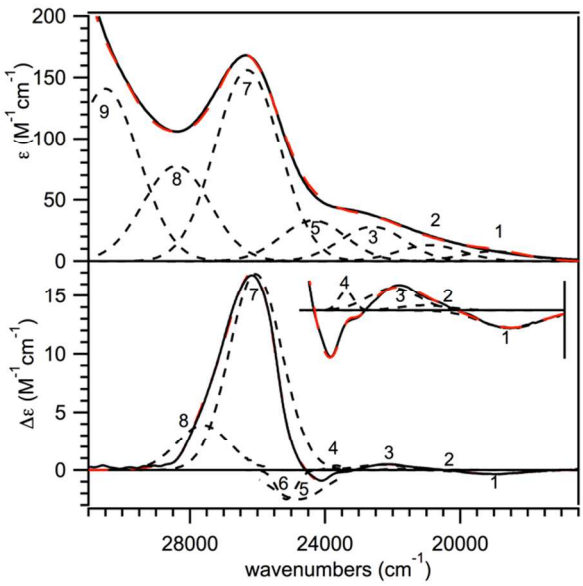

Figure 5. 298 K electronic absorption (top) and 2 K, 7 T MCD (bottom) spectra of $[Mn^{III}(O_2)(Tp^{Ph2})(THF)]$. Inset: An 15-fold enhancement of the 2 K, 7 T MCD spectra from 17 500 to 25 000 cm^{-1}. Individual Gaussian curves (black dotted lines) and their sums (red dashed lines) obtained from iterative fits of these data sets are displayed on their respective spectra. Only Gaussian bands 1 – 4 are shown in the inset. Conditions: Absorption data were collected for a 2.5 mM sample in THF. MCD data were collected for a 15 mM frozen glass sample in 75:25 solution of 2-Me-THF:THF.

and suggest that these transitions are intra-configurational. Bands 1, 3, 5, and 7 exhibit high to moderate intensity in the MCD spectrum and are assigned as the four ligand-field *d-d* transitions expected for an $S = 2$ Mn^{III} center (Table 5, Figure 6). Here, we note that the high energy of band 1 (19 000 cm^{-1}), which is the lowest-energy *d-d* transition, makes $[Mn^{III}(O_2)(Tp^{Ph2})(THF)]$ unique compared to peroxomanganese(III) species supported by the tetradentate bis(pyridyl)- and bis(quinolinyl)-diazepane ligands, where the corresponding transition ranged from 13 650 – 16 630.[16,18,32] For that series of complexes, this variation was related to slight differences in one $Mn–O_{peroxo}$ distance (1.869 – 1.907 Å). Because the $Mn–O_{peroxo}$ distances of $[Mn^{III}(O_2)(Tp^{Ph2})(THF)]$ fall within this range (see Table 4), another structural perturbation must account for the high energy of band 1 in this case.

Table 5. MCD, electronic absorption, calculated TD-DFT, and NEVPT2 electronic transition energies (cm^{-1}) of $[Mn^{III}(O_2)(Tp^{Ph2})(THF)]$. Corresponding oscillator strengths are included in ESI, Table S14.

	Experimental		Calculated		
Band	Abs.	MCD	TD-DFT	NEVPT2	Assignment
1	19 000	19 000	20 500	25 700	d_{z^2} - d_{xy}[c]
2	20 890	21 455	23 300	-	CT[d]
3	22 600	22 325	27 200	29 500	d_{yz} - d_{xy}[c]
4	-[a]	23 675	-	26 800[b]	SF[b]
5	24 350	24 800	28 800	31 600	$d_{x^2-y^2}$ - d_{xy}[c]
6	-[a]	25 150	-	30 500[b]	SF[b]
7	26 300	26 060	30 600	32 000	d_{xz} - d_{xy}[c]
8	28 400	27 609	29 500	-	CT[d]
9	28 350		29 800	-	CT[d, e]

[a]Band only apparent in low-temperature, 7 T MCD spectrum. [b]Mn^{III} spin-forbidden *d-d* transitions to triplet excited states [c]Assigned as a spin-allowed transition involving primarily the Mn 3*d* orbitals as indicated. [d]Assigned as peroxo-to-manganese(III) charge transfer transition. [e]Based on the low MCD intensity of band 9, this feature could arise from a Tp^{Ph2}-based charge-transfer transition.

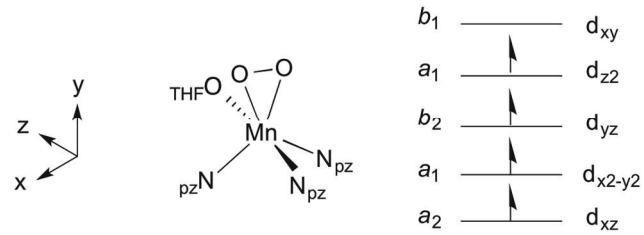

Figure 6. First coordination sphere of $[Mn^{III}(O_2)(Tp^{Ph2})(THF)]$ and *D*-tensor coordinate system from CP-DFT computations. The C_{2v} symmetry labels for the Mn 3*d* orbitals using the *D*-tensor coordinate system are provided.

VTVH MCD spectroscopy[37,61] was used to probe both the ZFS parameters and transition polarizations of $[Mn^{III}(O_2)(Tp^{Ph2})(THF)]$. VTVH MCD curves obtained for $[Mn^{III}(O_2)(Tp^{Ph2})(THF)]$ at 26 180 cm^{-1} are nested, indicating a moderate ZFS of the Mn^{III} ion (Figure 7) and were systematically fitted to obtain zero field splitting parameters. The best fits (χ^2 < 0.04) were obtained with D = -2.0 cm^{-1}, E/D = 0.05 and a predominant *z*- polarization (<1% *x*, <1% *y*-, and 98% *z*-polarization). These ZFS parameters are in excellent agreement with those obtained from the EPR data (D = -2.0(5) cm^{-1}; E/D = 0.07(1). In addition, these ZFS splitting parameters fall in the range of those reported for other peroxomanganese(III) adducts (D = -1.5 to -3.0 and E/D = 0.05 to 0.30).[16,19,20,25] Thus, the ZFS parameters of $[Mn^{III}(O_2)(Tp^{Ph2})(THF)]$ are not reflective of the unique τ parameter of this complex.

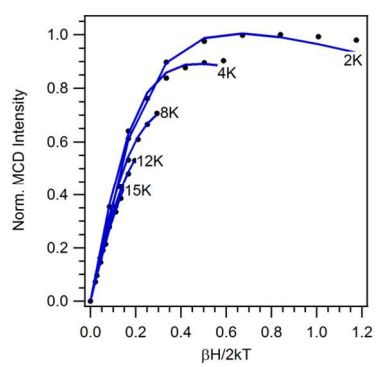

Figure 7. Experimental VTVH MCD data collected at 26 180 cm^{-1} for $[Mn^{III}(O_2)(Tp^{Ph2})(THF)]$ (⋯) and theoretical fit (—) using the following parameters: D = -2.00, E/D = 0.05, g_{iso} = 2.00, and 0.8% *x*, 0.8% *y*, and 98.4% *z* polarization.

X-ray Absorption Spectroscopy of $[Mn^{II}(Tp^{Ph2})(DMF)_3](OTf)$ and $[Mn^{III}(O_2)(Tp^{Ph2})(THF)]$

Dalton Transactions Accepted Manuscript

The Mn K-edge X-ray absorption data of $[Mn^{II}(Tp^{Ph2})(DMF)_3](OTf)$ shows a rising edge at 6547.5 eV, characteristic of a Mn^{II} species,[62,63] as well as a pre-edge feature at 6540.6 eV (ESI, Figure S6). The Fourier transform of the extended X-ray absorption fine structure (EXAFS) data of $[Mn^{II}(Tp^{Ph2})(DMF)_3](OTf)$ exhibits a primary peak at $R' = 1.7$ Å which was best fit with a shell of 3 O atoms at 2.16 Å and a shell of 3 N atoms at 2.28 Å (Figure 8, Table 6). Two smaller peaks are present in the Fourier transform at $R' = 2.5$ and 3.1 which were fit with a shell of 4 N atoms at 3.09 Å, a shell of 1 B atom at 3.33 Å, and a shell of 6 C atoms at 3.49 Å. The fits of the EXAFS data show excellent agreement with the bond lengths determined through XRD, particularly with the EXAFS fits of the average Mn-N and Mn-O distances of 2.28 and 2.16 Å, respectively (ESI, Table S10).

Table 6. EXAFS Fitting Results for $[Mn^{II}(Tp^{Ph2})(DMF)_3](OTf)$.[a]

	Mn-O			Mn-N			Mn-N			Mn-B			Mn-C			
Fit[b]	*n*	*r*(Å)	σ² (Å²)[c]	*n*	*r*(Å)	σ² (Å²)[c]	*n*	*r*(Å)	σ² (Å²)[c]	*n*	*r*(Å)	σ² (Å²)[c]	*n*	*r*(Å)	σ² (Å²)[c]	F-factor
1	6	2.18	7.41													0.612
2	3	2.14	3.29	3	2.26	2.58										0.598
3	3	2.14	3.53	3	2.26	2.84	5	3.10	3.14							0.552
10	3	2.16	3.88	3	2.27	3.53	3	3.08	0.60	1	3.30	6.05				0.535
15	***3***	***2.16***	***3.42***	***3***	***2.28***	***3.17***	***4***	***3.09***	***2.09***	***1***	***3.33***	***2.40***	***6***	***3.49***	***5.51***	***0.534***

[a]Fourier transform range is 2 – 14.5 Å (resolution 0.126 Å). [b]The fit number refers to all fits considered; see ESI Table S11. [c]Debye-waller factors are scaled × 10^3.

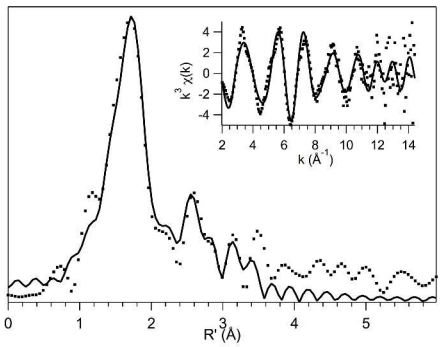

Figure 8. Fourier transform of Mn K-edge EXAFS data [$k^3\chi(k)$] and raw EXAFS spectra (insets), experimental data (···) and fits (–) for $[Mn^{II}(Tp^{Ph2})(DMF)_3](OTf)$.

We also attempted to collect Mn K-edge X-ray absorption data for $[Mn^{III}(O_2)(Tp^{Ph2})(THF)]$; however, all datasets showed signs of photoreduction or sample degradation which was evident by a shift in the edge energy and disappearance of the pre-edge feature (ESI, Figure S7). Several attempts were made to circumvent the sample instability, such as preparation with different solvents (50:50 mixture of 2-Me-tetrahydrofuran:THF, THF, and toluene) and by several methods of preparation, but sample degradation was observed in all cases when the sample was subjected to the X-ray beam.

Ligand Exchange Reactions of $[Mn^{III}(O_2)(Tp^{Ph2})(THF)]$

The observation of the solvent (THF) ligand in the X-ray structure of $[Mn^{III}(O_2)(Tp^{Ph2})(THF)]$ appeared to present an opportunity to perform ligand substitution reactions *cis* to the Mn^{III}-O_2 unit, under the assumption that the THF ligand might be labile. In a peroxomanganese(III) complex supported by the 13-TMC ligand (Scheme 1), substitution *trans* to the Mn^{III}-O_2 unit has been successful with anionic ligands.[14] Ligand substitution with a series of tetraalkylammonium salts (NR_4X; where X = N_3 and F) as well as pyridine-N-oxide was attempted by treating $[Mn^{III}(O_2)(Tp^{Ph2})(THF)]$ with an excess (100 equivalents) of NR_4X or pyridine-N-oxide at 25 ºC. In all cases, no change in the optical signatures of $[Mn^{III}(O_2)(Tp^{Ph2})(THF)]$ were observed, and ESI-MS experiments on aliquots of a solution of $[Mn^{III}(O_2)(Tp^{Ph2})(THF)]$ after addition of NR_4X provided no evidence for the formation of $[Mn^{III}(O_2)(Tp^{Ph2})(X)]^-$ complexes.

DFT Computations and Electronic Structure of $[Mn^{III}(O_2)(Tp^{Ph2})(THF)]$

DFT computations were performed to provide a detailed comparison of the electronic structure of $[Mn^{III}(O_2)(Tp^{Ph2})(THF)]$with that of other peroxomanganese(III) adducts. The DFT-geometry-optimized model of $[Mn^{III}(O_2)(Tp^{Ph2})(THF)]$ has metal-ligand bond lengths very similar to those observed crystallographically (Figure 9, top left panel). In particular, the Mn–O_{peroxo} distances are within 0.03 Å of their crystallographic values (calculated: 1.881 and 1.894 Å; XRD: 1.859(2) and 1.865(2) Å). The calculated Mn–N distances are all predicted to be slightly larger than their crystallographic counterparts but all are within 0.07 Å of the experimental values. The Mn–O(THF) bond length shows a difference of in 0.04 Å between experimental and computed values. Overall, all calculated metric parameters are in quite acceptable agreement with the XRD structure of $[Mn^{III}(O_2)(Tp^{Ph2})(THF)]$.

Coupled-perturbed (CP) DFT calculations afforded the *D*-tensor orientation for $[Mn^{III}(O_2)(Tp^{Ph2})(THF)]$, (Figure 9, top left panel). The elongated N(1)–Mn–O(3) axis (see Figure 3 for atom numbering scheme) defines the *z*-axis of the *D*-tensor, and the *y*-axis bisects the O–O bond vector. The CP-DFT calculated ZFS parameters were $D = -1.37$ cm^{-1} and $E/D = 0.06$. Although the CP-DFT method slightly underestimates the magnitude of *D* relative to the experimental value of -2.0 cm^{-1}, the relative magnitude agrees well with experimental value of *D* observed for other Mn^{III}-O_2 adducts[23] and is smaller than *D* values of other non-peroxo Mn^{III} species (-4 to -5 cm^{-1}).[64,65] *E/D* is in excellent agreement with experiment (0.05 - 0.08). The CP-DFT computations also reveal that the dominant contribution to *D* is through spin-orbit coupling (D_{SOC}), although the spin-spin coupling contribution is certainly non-negligible (D_{SS} = -0.32 cm^{-1}). Additionally, D_{SOC} was also calculated using the state-

Dalton Transactions Accepted Manuscript

This journal is © The Royal Society of Chemistry [year]

averaged CASSCF/NEVPT2 method. In this case D is overestimated (D_{SOC} = -2.91 cm^{-1}) and the system is predicted to be too rhombic (E/D = 0.28). The CASSCF/NEVPT2 method calculated a 29% contribution to D_{SOC} in the same sign (-) from components of the lowest-lying $^3T_1$ state (from parent O_h symmetry) at 18 400, 19 200, and 20 400 cm^{-1}. Similarly, 30% total contribution to D_{SOC} comes from the lowest-lying quintet states at 25 700 and 29 500 cm^{-1}. Additionally, a ^3A state at 30 500 cm^{-1} contributed 27% to D as well as 99% to E. Contributions from individual excited states are listed in ESI, Table S15.

Before discussing spectral assignments for [Mn^{III}(O$_2$)(Tp^{Ph2})(THF)], we describe the bonding in this complex, focusing on the frontier MOs. In the D-tensor orientation, both the spin-up and spin-down Mn^{III} 3d_{xy}-based MOs (218α and 230β) are unoccupied and involved in Mn^{III}-O$_2$ σ-antibonding interactions (Figure 9, top right panel). The Mn^{III}-O$_2$ π-antibonding interaction is distributed over the Mn^{III} 3$d_{x^2-y^2}$- (195α, 197α, 200α, 201α, and 219β) and 3d_{yz}- (199α, and 225β) based MOs. For the 3$d_{x^2-y^2}$- and 3d_{yz}-based MOs, only the α-spin MOs are occupied. The strong σ-covalency of the Mn^{III}-O$_2$ unit is exemplified by the 34% Mn 3d and 52% O$_2$ p character in the α-spin Mn 3d_{xy} MO (218α), which is essentially identical to that calculated for other six-coordinate Mn^{III}-O$_2$ complexes using the same level of theory.[16] The Mn 3d_z^2-based MO of [Mn^{III}(O$_2$)(Tp^{Ph2})(THF)] largely reflects σ-interactions between the Mn–N(Tp) and Mn–O(THF) groups. The α-spin Mn 3d_z^2 MO carries 21% Mn 3d, 23% N(Tp^{Ph2}) 2p, 2% O(THF) 2p, and 3% O$_{peroxo}$ 2p character.

To develop detailed band assignments of the electronic transitions observed in the experimental absorption and MCD spectra (Figure 5, Table 5), electronic transition energies and intensities of [Mn^{III}(O$_2$)(Tp^{Ph2})(THF)] were calculated with the TD-DFT method. Overall, the TD-DFT calculated absorption spectrum for [Mn^{III}(O$_2$)(Tp^{Ph2})(THF)] shows good, qualitative agreement with the experimental absorption spectrum albeit with

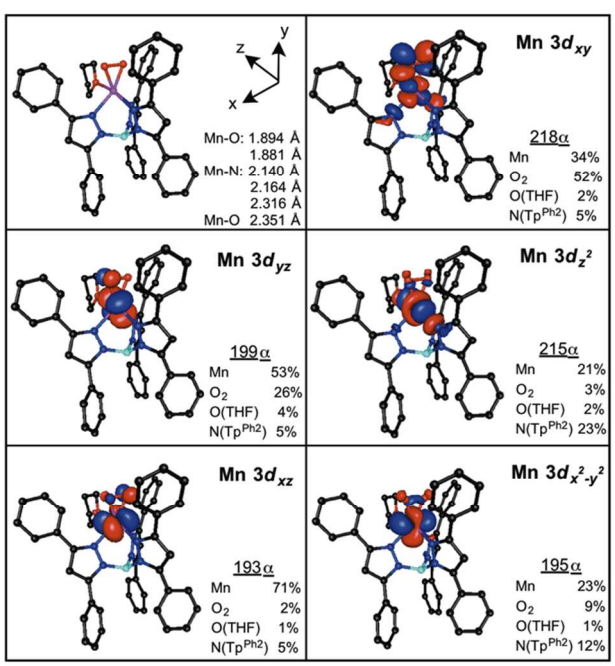

Figure 9. DFT-optimized structure of [Mn^{III}(O$_2$)(Tp^{Ph2})(THF)], with metal-ligand bond lengths and the D-tensor coordinate system from CP-DFT computations (top left panel), and surface contour plots of quasi-restricted Mn 3d-based orbitals (QROs). The sums of Mn 3d and ligand 2p contributions to the spin-up Kohn-Sham orbitals are listed next to the plots of the corresponding QROs.

a consistent overestimation of transition energies. In the experimental absorption spectrum of [Mn^{III}(O$_2$)(Tp^{Ph2})(THF)], three absorption envelopes are observed (regions A, B, and C; see Figure 10). Region A, which extends from 18 000 to 25 000 cm^{-1} in the experimental absorption spectrum contains contributions from bands 1 – 5. In the TD-DFT-calculated spectrum, region A contains contributions from the lowest-energy spin-allowed Mn^{III} d-d transition (state 2: $d_z^2 \rightarrow d_{xy}$; see Tables 5 and S12) at 20 500 cm^{-1} as well as a set of three peroxo-to-manganese(III) CT transitions from 23 000 to 25 500 cm^{-1} (states 3, 4, and 5). The calculated energy for the $d_z^2 \rightarrow d_{xy}$ transition is in excellent agreement with the experimental energy of band 1 (Table 5). Compared to other previously characterized peroxomanganese(III) species, the energy of the $d_z^2 \rightarrow d_{xy}$ transition is significantly shifted to higher energy. The peroxo-to-manganese(III) CT transitions in region A originate in the peroxo π* orbitals that are perpendicular, or out-of-plane, with respect to the Mn^{III}-O$_2$ unit (π_{op}*) and terminate in the spin-down Mn^{III} 3d-based MOs. However, these transitions are highly mixed, and this could account for the erroneously high TD-DFT-computed absorption intensity in this region. Nonetheless, these computations lend credence to the assignment of band 2 as a peroxo-to-manganese(III) CT transition.

Region B of the TD-DFT- computed absorption spectrum extends from 25 000 to 31 000 cm^{-1}. This region contains contributions from the three remaining spin-allowed Mn^{III} d-d transitions ($d_{yz} \rightarrow d_{xy}$, state 8; $d_{x^2-y^2} \rightarrow d_{xy}$, state 12; and $d_{xz} \rightarrow d_{xy}$,

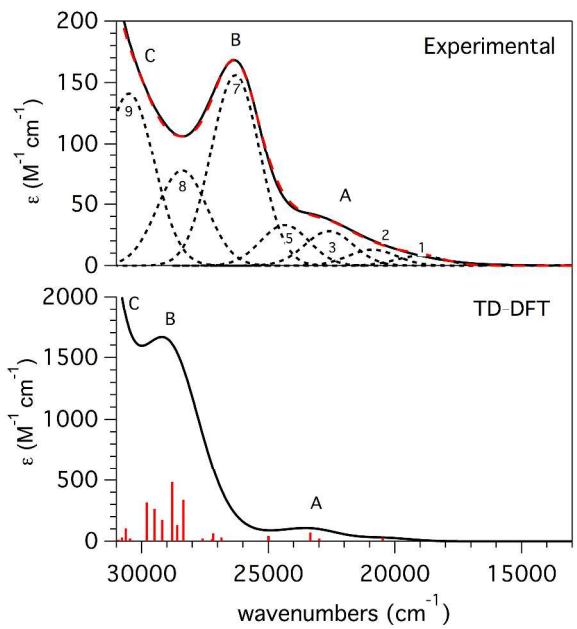

Figure 10. Experimental (top) and TD-DFT-calculated (bottom) absorption spectra of [Mn^{III}(O$_2$)(Tp^{Ph2})(THF)].

Dalton Transactions Accepted Manuscript

state 17), as well as additional peroxo-to-manganese(III) charge transfer transitions (Tables 5 and S12).[66] Compared to experiment, transitions in region B are calculated at too high an energy by ~5 000 cm^{-1}. Nonetheless, these calculations are generally supportive of the spectral assignments discussed previously. Additionally, state 17 is composed of the $d_{xz} \rightarrow d_{xy}$ transition, which corresponds to a *z*-polarized $^4B_1 \rightarrow {}^4A_2$ transition using the *D*-tensor coordinate system (Figure 6) and assuming idealized C_{2v} symmetry, with the *y*-axis as the pseudo-C_2 axis. This corroborates the assignment of band 7 as a $d_{xz} \rightarrow d_{xy}$ transition, as band 7 was characterized by VTVH MCD to be 98% *z*-polarized.

Region C of the TD-DFT absorption spectrum is composed of peroxo-to-manganese(III) CT transitions with contributions from states 14 (29 500 cm^{-1}) and 15 (29 800 cm^{-1}). TD-DFT calculations incorrectly predict the ordering of these CT states with respect to the highest-energy *d-d* transition (state 17, 30 600 cm^{-1}), however, this is not unusual for TD-DFT calculations.

Additionally, the excited state energies of $[Mn^{III}(O_2)(Tp^{Ph2})(THF)]$ were calculated by the CASSCF/NEVPT2 method to exclude the possibility of TD-DFT-calculated charge-transfer states with erroneously high intensity and low energy (so-called "intruder states"), that can occur as artifacts. The CASSCF/NEVPT2 method also has the advantage that spin-forbidden excited states can be treated. The *d-d* excited states from the CASSCF/NEVPT2 calculations agree well with the TD-DFT energies, confirming the presence of few intruder states in the latter spectrum. Importantly, two triplet excited states are predicted with energies (26 800 and 30 500 cm^{-1}) that interleave the quartet excited state energies (Table 5), supporting our assignment of bands 4 and 6 as spin-forbidden transitions. It should be noted that the TD-DFT method predicts a significant contribution to region B from state 10 in the TD-DFT calculations (Table S13); however, state 10 is predicted as a $Ph(Tp^{2Ph}) \rightarrow Mn$ intruder state. This transition is an anticipated artifact of the TD-DFT calculation and is not expected to contribute to the experimental absorption spectrum.

DFT Computations and Electronic Structure of the Blue and Brown Isomers of $[Mn^{III}(O_2)(Tp^{iPr2})(pz^{iPr2}H)]$

Due to the reasonable success in reproducing the spectroscopic properties of $[Mn^{III}(O_2)(Tp^{Ph2})(THF)]$ with these computational methods, a similar approach was utilized for the isomers of $[Mn^{III}(O_2)(Tp^{iPr2})(pz^{iPr2}H)]$ in an attempt to explain the thermochromic shift in the electronic absorption spectrum. The 22 nm (670 cm^{-1}) red shift in the electronic absorption spectrum upon cooling from 253 to 193 K was associated with the formation of a hydrogen bond between the pyrazole ligand and one O atom of the peroxo unit in the low-temperature isomer. TD-DFT calculations were performed on models of $[Mn^{III}(O_2)(Tp^{iPr2})(pz^{iPr2}H)]$ built using the XRD coordinates of the isomers at 253 and 193 K (brown and blue isomers, respectively) in order to elucidate the nature of the changes in the absorption spectrum by determining the electronic structure. TD-DFT calculations were performed with both the unmodified XRD coordinates, as well as structures where the positions of the hydrogen atoms were optimized. Primarily, the optimization of the hydrogen atoms resulted in a shorter hydrogen bond, with a 0.139 Å decrease between the H-donor atom and the O(peroxo) acceptor in the blue isomer and a corresponding decrease of 0.049 Å in the brown isomer (Table 7).

TD-DFT calculations with both the hydrogen-optimized and XRD structures reproduce the experimental absorption spectra well. TD-DFT calculations performed with the XRD coordinates

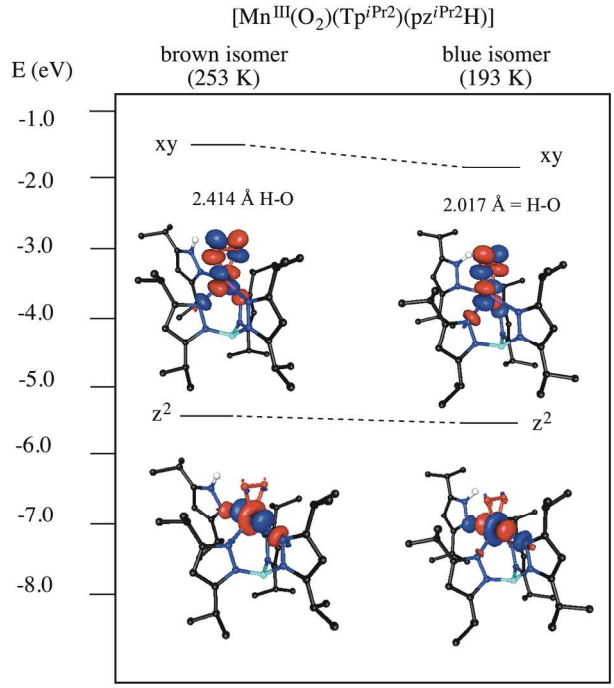

Figure 11. TD-DFT-calculated donor and acceptor orbitals for the lowest energy *d-d* transition in the brown and blue isomers of $[Mn^{III}(O_2)(Tp^{iPr2})(pz^{iPr2}H)]$. For clarity, all hydrogens except the hydrogen- bonding $H_{pyrazole}$ have been omitted.

Table 7. Selected Bond Lengths (Å) for $[Mn^{III}(O_2)(Tp^{iPr2})(pz^{iPr2}H)]$ for fully-optimized coordinates, unmodified XRD coordinates, and hydrogen-optimized coordinates.

Full Optimization	H-O[a]	N-H	O-O	Mn-O	Mn-O
blue	1.891	1.039	1.450	1.910	1.858
brown	1.890	1.039	1.450	1.858	1.910
XRD Coordinates[22]	H-O	N-H	O-O	Mn-O	Mn-O
blue	2.156	0.975	1.434	1.880	1.844
brown	2.464	0.977	1.429	1.850	1.851
Hydrogen Optimized	H-O	N-H	O-O	Mn-O	Mn-O
blue	2.017	1.033	1.434	1.880	1.844
brown	2.414	1.026	1.429	1.850	1.851

[a]H-O bond length listed is the shortest of the H-O bond lengths calculated.

predict a transition at 18 500 cm^{-1} for the brown isomer and a transition at 17 300 cm^{-1} for the blue isomer, in good agreement with the experimental values (17 820 and 17 150 cm^{-1}). The transition energies obtained through TD-DFT calculations with the hydrogen-optimized structures were at slightly higher energies of 18 900 and 17 500 cm^{-1} for the blue and brown

Dalton Transactions Accepted Manuscript

This journal is © The Royal Society of Chemistry [year]

isomers, respectively. Importantly, both the XRD and the hydrogen-optimized structures reproduce the red-shift that occurs as the complex is cooled from 253 to 193 K. With all TD-DFT calculations, this red-shifted transition involves a one-electron excitation between the α-spin Mn $3d_{z^2}$ MO (190α), which is highly mixed, and the unoccupied α-spin Mn $3d_{xy}$ MO 192α). The acceptor orbital exhibits strong σ-covalency of the Mn^{III}-O_2 unit, with 42 - 45% Mn 3*d* and 44 – 47% O_2 2*p* character (ESI, Tables S16 - S19), which is similar to other previously characterized Mn^{III}-O_2 complexes. The band shift in the experimental absorption spectrum of the blue isomer of $[Mn^{III}(O_2)(Tp^{iPr2})(pz^{iPr2}H)]$ is due to the stabilization of the Mn $3d_{xy}$ acceptor MO, which carries significant peroxo ligand character, with the formation of the hydrogen bond (Figure 11). The hydrogen-optimized structure of the blue isomer exhibits the shortest hydrogen bond at 2.017 Å which is accompanied by the greatest stabilization of 0.2294 eV of the Mn $3d_{xy}$ acceptor MO (192 α) relative to the corresponding orbital of the brown isomer (Table 7, Figure 11). TD-DFT calculations with the unmodified XRD structures display a similar trend with the blue isomer showing a hydrogen bond of 2.156 Å and a stabilization of the acceptor MO in the blue isomer of 0.1679 eV relative to the brown isomer. Notably, when both the brown and blue isomers were fully optimized (*i.e.* the positions of all atoms were energy-minimized), the computations yielded isomeric structures with a hydrogen bond distances of 1.891 and 1.890 Å and equivalent Mn—O distances of 1.858 and 1.910 Å (Table 7).

Discussion

Although there have been a variety of synthetic peroxomanganese(III) species supported by anionic ligands,[14,22,25] there is still a lack of detailed bonding descriptions of such complexes. In particular, peroxomanganese(III) species supported by monoanionic and facially coordinating Tp ligands exhibit unusual electronic absorption spectra that have been unexplained by studies to date. In order to investigate the electronic structure of one of these species, a monomeric Mn^{III}-O_2 adduct supported by the Tp^{Ph2} ligand was synthesized and characterized by XRD, EPR, and MCD spectroscopies as well as TD-DFT and CASSCF/NEVPT2 computations. The high thermal stability of $[Mn^{III}(O_2)(Tp^{Ph2})(THF)]$, presumably due in part to the steric bulk of the phenyl groups of the Tp^{Ph2} ligand shielding the peroxo moiety, facilitated the determination of the crystal structure.

The XRD structure of $[Mn^{III}(O_2)(Tp^{Ph2})(THF)]$ shows metric parameters in line with those collected for other peroxomanganese(III) species.[23] The Mn^{III} oxidation state was confirmed by EPR spectroscopy. Previously characterized peroxomanganese(III) species exhibit 6-line signals at ~80 mT with hyperfine splitting of 6-7 mT.[23] As $[Mn^{III}(O_2)(Tp^{Ph2})(THF)]$ displays a feature position of 84.6 mT and a hyperfine splitting of 5.1 mT. This hyperfine splitting is somewhat smaller than those of other non-peroxo manganese(III) species[67,68] and previously studied peroxomanganese(III) adducts[23], possibly suggesting a higher degree of covalency in the $[Mn^{III}(O_2)(Tp^{Ph2})(THF)]$ complex. Temperature dependence studies and simulation of the parallel-mode EPR feature yielded D = -2.0(5) cm^{-1} and E/D = 0.07(1), which are very similar to the ZFS parameters for other Mn^{III}-O_2 species which lie between -1.5 and -3.0 cm^{-1} for D and 0.05 to 0.30 for E/D.[23] In addition to supporting the assignment of this intermediate as a Mn^{III} species, the determination of these zero field splitting parameters for $[Mn^{III}(O_2)(Tp^{Ph2})(THF)]$ supply insight into the ground state properties of Mn^{III}-O_2 species.

To elucidate the origin of the blue-shift observed in the absorption spectrum of $[Mn^{III}(O_2)(Tp^{Ph2})(THF)]$ compared to other members of the Mn^{III}-O_2 class of intermediates, we turned to MCD spectroscopy and TD-DFT calculations. Although we have previously attributed slight variations in the lowest-energy ligand-field transitions of Mn^{III}-O_2 adducts to differences in the the Mn—O_{peroxo} bond length,[16,18,32] this correlation fails here, as the Mn—O_{peroxo} distances of $[Mn^{III}(O_2)(Tp^{Ph2})(THF)]$ are within the range of Mn—O_{peroxo} bond lengths observed in the prior series. Instead, the high energy of band 1 in the MCD and electronic absorption spectra of $[Mn^{III}(O_2)(Tp^{Ph2})(THF)]$ (Figure 5) results from perturbations perpendicular to the Mn^{III}-O_2 unit. Specifically, elongation in the N(1)—Mn—O(3) bonding axis (Figure 9, top left panel), which is a result of weak σ-donation from the THF ligand, stabilizes the $3d_{z^2}$ MO and blue-shifts the $3d_{xy} \rightarrow 3d_{z^2}$ transition. This is reflected in the experimentally determined ligand-field excited state energies of $[Mn^{III}(O_2)(Tp^{Ph2})(THF)]$ compared to other Mn^{III}-O_2 species (Figure 12). The $3d_{xy}$ - $3d_{z^2}$ energy gap, $\Delta(3d_{xy} - 3d_{z^2})$, in $[Mn^{III}(O_2)(Tp^{Ph2})(THF)]$ is 4.5 eV, whereas $\Delta(3d_{xy} - 3d_{z^2})$ is 4.1 and 3.8 eV for the Mn^{III}-O_2 complexes $[Mn^{III}(O_2)(L^7py_2^H)]^+$ and $[Mn^{III}(O_2)(L^7py_2^{6\text{-}Me})]^+$, respectively ($L^7py_2^H$ and $L^7py_2^{Me}$ are neutral N_4 ligands).

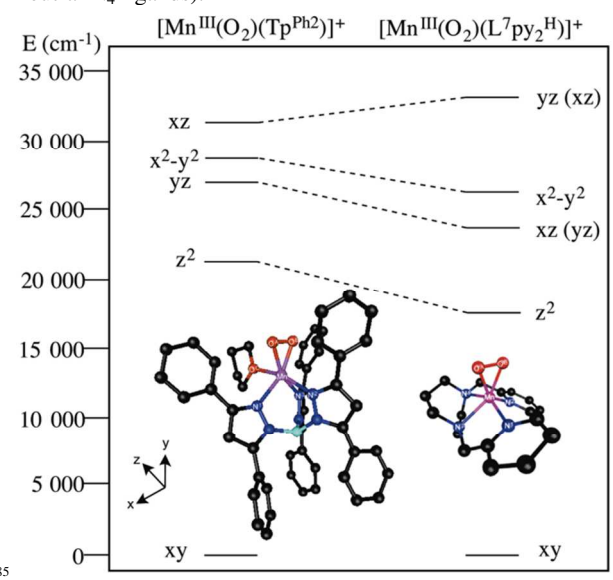

Figure 12. TD-DFT calculated *d-d* transitions in $[Mn^{III}(O_2)(Tp^{Ph2})(THF)]$ and $[Mn^{III}(O_2)(L^7py_2^H)]^+$. Following the hole formalism for these d^4 systems, the excited state is designated according to the *d* orbital hole. In *D*-tensor orientation of the $[Mn^{III}(O_2)(L^7py_2^H)]^+$ model, the *x* and *y* axes are swapped relative to $[Mn^{III}(O_2)(Tp^{Ph2})(THF)]$; the orbital labels corresponding to the coordinate system of $[Mn^{III}(O_2)(Tp^{Ph2})(THF)]$ are shown in parentheses.

In our computational investigations of $[Mn^{III}(O_2)(Tp^{Ph2})(THF)]$, two methods, TD-DFT and CASSCF/NEVPT2, were used to calculate electronic transitions energies. The more commonly used TD-DFT method is known to potentially introduce intruder states that do not contribute to the

Dalton Transactions Accepted Manuscript

experimental spectrum. In general, the CASSCF/NEVPT2 method is accepted as a more reliable method for treating the excited states of transition metal complexes. In this present case, both methods overestimated the electronic transition energies compared to the experimentally observed bands, with the TD-DFT-calculated energies being closer to the experimental values. However, below 32 000 cm^{-1}, the absorption spectra of $[Mn^{III}(O_2)(Tp^{Ph2})(THF)]$ calculated by both methods are comparable in their replication of the experimental spectrum with the exception of one intruder state in the TD-DFT calculation, which had a negligible effect on the primary features of the computed absorption spectrum. Here, TD-DFT calculations were sufficient to predict the electronic absorption spectrum, particularly the *d-d* transitions, and the use of the more input-rigorous CASSCF/NEVPT2 method may not be necessary in other similar cases.

TD-DFT calculations were extended to investigate the brown and blue isomers of $[Mn^{III}(O_2)(Tp^{iPr2})(pz^{iPr2}H)]$. As previously reported, when the $[Mn^{III}(O_2)(Tp^{iPr2})(pz^{iPr2}H)]$ species is cooled from 253 to 193 K, a hydrogen bond between the pyrazole ligand and one O atom of the peroxo unit is formed, and the absorption spectrum exhibits a 670 cm^{-1} red-shift. TD-DFT calculations permit the assignment of the red-shifted electronic transition to a Mn $d_{z^2} \rightarrow d_{xy}$ one-electron excitation. The Mn $3d_{xy}$ acceptor MO of both isomers contains a significant amount of peroxo ligand character. The hydrogen bonding interaction with the peroxo moiety, and the concomitant Mn-O bond elongation, stabilizes this MO in the blue isomer by 0.2294 eV relative to the brown isomer (Figure 11).

The stabilization of the Mn-O_2 σ-antibonding $3d_{xy}$ MO through a hydrogen-bonding interaction is of potential relevance to two recent reports describing activation of Mn^{III}-O_2 adducts through chemical and electrochemical reduction. Using a Mn^{III}-O_2 adduct supported by a trianionic tripodal ligand with a hydrogen-bonding cavity around the peroxo, Borovik and co-workers showed that the two-electron reduction of a Mn^{III}-O_2 adduct using diphenylhydrazine led to O-O bond cleavage and the eventual formation of a hybrid oxo-/hydroxo-manganese(III) adduct.[69,26] A dihydroxomanganese(III) species was postulated as an intermediate in this process. These elementary steps feature in the catalytic reduction of O_2 to H_2O by the corresponding Mn^{II} complex. In a separate study, Anxolabéhère-Mallart, Policar, and Robert reported that the two-electron electrochemical reduction of a Mn^{III}-O_2 adduct supported by a phenolate-containing N_4O^- ligand (the protonated, phenol form of the ligand is *N*-)2-hydroxybenzyl)-*N*,*N'*-bis[2-(*N*-methylimidazolyl)methyl]ethane-1,2-diamine) causes O-O bond cleavage when the reduction is carried out in the presence of water.[70] Detailed electrochemical studies revealed that this process is kinetically controlled by the initial electron transfer that is also associated with a large reorganization energy. In both systems, hydrogen bonding to the peroxo ligand, either intramolecular with the supporting ligand or intermolecular with added water, is possible. On the basis of our computational work described here, hydrogen-bonding to the peroxo of a Mn^{III}-O_2 unit stabilizes the Mn $3d_{xy}$ orbital (Figure 11), which is the spin-α LUMO, potentially facilitating reduction of the Mn^{III}-O_2 unit. Because this MO contains a significant percentage of peroxo π* character, the addition of an electron to this MO would weaken the O-O bond, priming it for cleavage.

Conclusions

The conversion of $[Mn^{II}(Tp^{Ph2})(DMF)_3](OTf)$ to $[Mn^{III}(O_2)(Tp^{Ph2})(THF)]$ by KO_2 yielded a peroxomanganese(III) species exhibiting high thermal stability with unique spectral features in both the electronic absorption and MCD spectra. The nature of these spectral deviations from previously characterized peroxomanganese(III) species arises from an axial elongation along the molecular z-axis, reducing the metal-ligand covalency, stabilizing the σ-antibonding Mn d_{z^2} MO, and affording higher energy *d-d* transitions. Comparably, in the peroxomanganese(III) species supported by the Tp^{iPr2} ligand, a hydrogen bonding interaction stabilizes the acceptor MO, causing the thermochromic shift observed as the complex is cooled from 293 to 193 K. These perturbations in the electronic transitions of these peroxomanganese(III) species represent an example of a deviation in symmetry and metal-ligand bonding in Mn^{III}-(O_2) intermediates and could be applied in the identification of similar changes in the first coordination sphere of short-lived intermediates in enzymatic and model systems.

Acknowledgements

This work was supported by the US NSF (CHE-1056470 to T.A.J.). XAS experiments were supported by the Center for Synchrotron Biosciences grant, P30-EB-009998, from the National Institute of Biomedical Imaging and Bioengineering (NIBIB). The US NSF is also acknowledged for funds used for the purchase of X-ray instruments (CHE-0079282) and the EPR spectrometer (CHE-0946883). H.E.C. was supported by NIH-GMS T32 GM08545. We thank Dr. Erik Farquhar at NSLS for outstanding support of our XAS experiments.

Notes and references

1251 Wescoe Hall Drive, Lawrence, KS, USA. Fax: 785 864 5693; Tel:+1 785 864 3968; E-mail: taj@ku.edu

† Electronic Supplementary Information (ESI) available: Crystal data and structure refinement information, variable-temperature electronic absorption spectra of $[Mn^{III}(O_2)(Tp^{Ph2})(THF)]$, temperature dependent EPR data for $[Mn^{III}(O_2)(Tp^{Ph2})(THF)]$, IR spectra of $[Mn^{II}(Tp^{Ph2})(DMF)_3](OTf)$ and $[Mn^{III}(O_2)(Tp^{Ph2})(THF)]$, variable-temperature 7T MCD spectra, deconvoluted MCD data, XAS spectra of $[Mn^{II}(Tp^{Ph2})(DMF)_3](OTf)$ and $[Mn^{III}(O_2)(Tp^{Ph2})(THF)]$, EXAFS fitting results for $[Mn^{II}(Tp^{Ph2})(DMF)_3](OTf)$, DFT-optimized cartesian coordinates, TD-DFT-calculated parameters, and CASSCF-NEVPT2-calculated parameters. CCDC reference numbers 1018686 and 1018687. See DOI: 10.1039/b000000x/.

(1) Grove, L. E.; Brunold, T. C. *Comments on Inorganic Chemistry* **2008**, *29*, 134.

(2) Miller, A.-F. *Curr. Opin. Chem. Biol.* **2004**, *8*, 162.

(3) Jackson, T. A.; Karapetian, A.; Miller, A.-F.; Brunold, T. C. *Biochemistry* **2005**, *44*, 1504.

(4) Bull, C.; Niederhoffer, E. C.; Yoshida, T.; Fee, J. A. *Journal of the American Chemical Society* **1991**, *113*, 4069.

Dalton Transactions Accepted Manuscript

This journal is © The Royal Society of Chemistry [year]

(5) Hearn, A. S.; Stroupe, M. E.; Cabelli, D. E.; Lepock, J. R.; Tainer, J. A.; Nick, H. S.; Silverman, D. N. *Biochemistry* **2001**, *40*, 12051.

(6) Hearn, A. S.; Tu, C. K.; Nick, H. S.; Silverman, D. N. *Journal of Biological Chemistry* **1999**, *274*, 24457.

(7) Gunderson, W. A.; Zatsman, A. I.; Emerson, J. P.; Farquhar, E. R.; Que, L.; Lipscomb, J. D.; Hendrich, M. P. *J. Am. Chem. Soc.* **2008**, *130*, 14465.

(8) Vetting, M. W.; Wackett, L. P.; Que, L., Jr.; Lipscomb, J. D.; Ohlendorf, D. H. *Journal of Bacteriology* **2004**, *186*, 1945.

(9) Opaleye, O.; Rose, R.-S.; Whittaker, M. M.; Woo, E.-J.; Whittaker, J. W.; Pickersgill, R. W. *Journal of Biological Chemistry* **2006**, *281*, 6428.

(10) Borowski, T.; Bassan, A.; Richards, N. G. J.; Siegbahn, P. E. M. *Journal of Chemical Theory and Computation* **2005**, *1*, 686.

(11) Reinhardt, L. A.; Svedruzic, D.; Chang, C. H.; Cleland, W. W.; Richards, N. G. J. *Journal of the American Chemical Society* **2003**, *125*, 1244.

(12) Svedružic, D.; Jónsoon, S.; Toyota, C. G.; Reinhardt, L. A.; Ricagno, S.; Lindqvist, Y.; Richards, N. G. J. *Archives of Biochemistry and Biophysics* **2005**, *433*, 176.

(13) Tanner, A.; Bowater, L.; Fairhurst, S. A.; Bornemann, S. *Journal of Biological Chemistry* **2001**, *276*, 43627.

(14) Annaraj, J.; Cho, J.; Lee, Y.-M.; Kim, S. Y.; Latifi, R.; de Visser, S. P.; Nam, W. *Angew. Chem. Int. Ed.* **2009**, *48*, 4150.

(15) Cho, J.; Sarangi, R.; Nam, W. *Acc. Chem. Res.* **2012**, *45*, 1321.

(16) Geiger, R. A.; Chattopadhyay, S.; Day, V. W.; Jackson, T. A. *Journal of the American Chemical Society* **2010**, *132*, 2821.

(17) Geiger, R. A.; Chattopadhyay, S.; Day, V. W.; Jackson, T. A. *Dalton Trans.* **2011**, *40*.

(18) Geiger, R. A.; Leto, D. F.; Chattopadhyay, S.; Dorlet, P.; Anxolabéhère-Mallart, E.; Jackson, T. A. *Inorganic Chemistry* **2011**, *50*, 10190.

(19) Groni, S.; Blain, G.; Guillot, R.; Policar, C.; Anxolabéhère-Mallart, E. *Inorganic Chemistry* **2007**, *46*, 1951.

(20) Groni, S.; Dorlet, P.; Blain, G.; Bourcier, S.; Guillot, R.; Anxolabéhère-Mallart, E. *Inorganic Chemistry* **2008**, *47*, 3166.

(21) Kang, H.; Cho, J.; Cho, K.-B.; Nomura, T.; Ogura, T.; Nam, W. *Chem. Eur* **2013**, *19*.

(22) Kitajima, N.; Komatsuzaki, H.; Hikichi, S.; Osawa, M.; Moro-oka, Y. *J. Am. Chem. Soc.* **1994**, *116*, 11596.

(23) Leto, D. F.; Jackson, T. A. *J. Biol. Inorg. Chem.* **2014**, *19*, 1.

(24) Seo, M. S.; Kim, J. Y.; Annaraj, J.; Kim, Y.; Lee, Y.-M.; Kim, S.-J.; Kim, J.; Nam, W. *Angewandte Chemie International Edition* **2007**, *46*, 377.

(25) Shook, R. L.; Gunderson, W. A.; Greaves, J.; Ziller, J. W.; Hendrich, M. P.; Borovik, A. S. *Journal of the American Chemical Society* **2008**, *130*, 8888.

(26) Shook, R. L.; Peterson, S. M.; Greaves, J.; Moore, C.; Rheingold, A. L.; Borovik, A. S. *J. Am. Chem. Soc.* **2011**, *133*, 5810.

(27) Singh, U. P.; Sharma, A. K.; Hikichi, S.; Komatsuzaki, H.; Moro-oka, Y.; Akita, M. *Inorganica Chimica Acta* **2006**, *359*, 4407.

(28) M.K., C.; Kovacs, J. A. *J. Am. Chem. Soc.* **2011**, *133*, 12470.

(29) Coggins, M. K.; V., M.-D.; S., D.; J.A., K. *J. Am. Chem. Soc.* **2013**, *135*.

(30) VanAtta, R. B.; Strouse, C. E.; Hanson, L. K.; Valentine, J. S. *Journal of the American Chemical Society* **1987**, *109*, 1425.

(31) For Mn^{III}-O_2 adducts, the τ parameter is used exclusively to compare angles between axial donors perpendicular to the Mn^{III}-O_2 unit with angles between equatorial donors parallel to the Mn^{III}-O_2 unit (Scheme 1). This differs somewhat from the conventional τ parameter used for authentic five-coordinate complexes. Most notably, τ values of greater than 1 are possible under the Mn^{III}-O_2 formalism.

(32) Geiger, R. A.; Wijeratne, G.; Day, V. W.; Jackson, T. A. *Eur. J. Inorg. Chem.* **2012**, 1598.

(33) Pecoraro, V. L.; Baldwin, M. J.; Gelasco, A. *Chem. Rev.* **1994**, *94*, 807.

(34) Vaska, L. *Acc. Chem. Res.* **1975**, *9*, 175.

(35) Sheldrick, G. M. Bruker-AXS 5465 E. Cheryl Parkway, Madison, WI 53711-5373 USA, 2000.

(36) Stoll, S.; Schweiger, A. *J. Magn. Reson.* **2006**, *178*, 42.

(37) Neese, F.; Solomon, E. I. *Inorganic Chemistry* **1999**, *38*, 1847.

(38) George, G. N. In *EXAFSPAK* Stanford Synchrotron Radiation Laboratory; Stanford, CA, 1990.

(39) Rehr, J. J.; Mustre de Leon, J.; Zabinsky, S. I.; Albers, R. C. *Journal of the American Chemical Society* **1991**, *113*, 5135.

(40) Neese, F., The ORCA program system, *Wiley Interdiscip. Rev.: Comput. Mol. Sci.* 2012, p 73.

(41) Becke, A. D. *J. Chem. Phys.* **1986**, *84*, 4524.

(42) Perdew, J. P. *Phys. Rev. B* **1986**, *33*, 8822.

(43) Schäfer, A.; Horn, H.; Ahlrichs, R. *J. Chem. Phys.* **1992**, *97*, 2571.

(44) Schäfer, A.; Huber, C.; Ahlrichs, R. *J. Chem. Phys.* **1994**, *100*, 5829.

(45) Neese, F. *Journal of Computational Chemistry* **2003**, *24*, 1740.

(46) Sinnecker, S.; Rajendran, A.; Klamt, A.; Diedenhofen, M.; Neese, F. *Journal of Physical Chemistry A* **2006**, *110*, 2235.

(47) Bauernschmitt, R.; Ahlrichs, R. *Chem. Phys. Lett.* **1996**, *256*, 454.

(48) Casida, E. M.; Jamorski, C.; Casida, K. C.; Salahub, D. R. *J. Chem. Phys.* **1998**, *108*, 4439.

(49) Stratman, R. E.; Scuseria, G. E.; Frisch, M. J. *J. Chem. Phys.* **1998**, *109*, 8218.

(50) Hirata, S.; Head-Gordon, M. *Chem. Phys. Lett.* **1999**, *302*, 375.

(51) Hirata, S.; Head-Gordon, M. *Chem. Phys. Lett.* **1999**, *314*, 291.

(52) Becke, A. D. *J. Chem. Phys.* **1993**, *98*, 1372.

(53) Becke, A. D. *J. Chem. Phys.* **1993**, *98*, 5648.

(54) Lee, C.; Yang, W.; Parr, R. G. *Phys. Rev. B* **1988**, *37*, 785.

(55) Angeli, C.; Cimiraglia, R.; Evangelisti, S.; Leininger, T.; Malrieu, J. P. *J. Chem. Phys.* **2001**, *114*, 10252.

(56) Hammes, B. S.; Carrano, M. W.; Carrano, C. J. *J. Chem. Soc., Dalton Trans.* **2001**, 1448.

(57) Singh, U. P.; Sharma, A. K.; Tyaji, P.; Upreti, S.; Singh, R. K. *Polyhedron* **2006**, *25*, 3628.

(58) Schultz, D. A.; Vostrikova, K. E.; Bodnar, S. H.; Koo, H.-J.; Whangbo, M.-H.; Kirk, M. L.; Depperman, E. C.; Kampf, J. W. *J. Am. Chem. Soc.* **2003**, *125*, 1607.

(59) Lever, A. B. P. *Inorganic Electronic Spectroscopy*; 2nd ed.; Elsevier: Amsterdam; New York, 1984.

Dalton Transactions Accepted Manuscript

(60) Band 9 has exceptionally low MCD intensity and could also be assigned as a TpPh2 to manganese(III) CT transition.

(61) Oganesyan, V. S.; George, S. J.; Cheesman, M. R.; Thomson, A. J. *J. Chem. Phys.* **1999**, *110*, 762.

(62) Leto, D. F.; Chattopadhyay, S.; Day, V. W.; Jackson, T. A. *Dalton Trans.* **2013**, *42*, 13014.

(63) Leto, D. F.; Jackson, T. A. *Inorg. Chem.* **2014**, *53*, 6179.

(64) Neese, F. *J. Am. Chem. Soc.* **2006**, *128*, 10213.

(65) Krzystek, J.; Ozarowski, A.; Telser, J. *Coordination Chemistry Reviews* **2006**, *250*, 2308.

(66) These transitions are all highly mixed, and the natures of the excited states were identified through visualization of electron density difference maps (EDDMs.

(67) Krivokapic, I.; Noble, C.; Klitgaard, S.; Tregenna-Piggott, P.; Weihe, H.; Barra, A.-L. *Angew. Chem. Int. Ed.* **2005**, *44*, 3613.

(68) Krzystek, J.; Yeagle, G. J.; Park, J.-H.; Britt, R. D.; Meisel, M. W.; Brunel, L.-C.; Joshua, T. *Inorg. Chem.* **2003**, *42*, 4610.

(69) The metric parameters in the crystal structure of this complex indicate that a proton is nearly equally shared between the supporting ligand and a coordinated oxygen atom.

(70) Ching, H. Y. V.; Anxolabéhère-Mallart, E.; Colmer, H. E.; Costentin, C.; Dorlet, P.; Jackson, T. A.; Policar, C.; Robert, M. *Chemical Science* **2014**, *5*.

Dalton Transactions Accepted Manuscript

This journal is © The Royal Society of Chemistry [year]

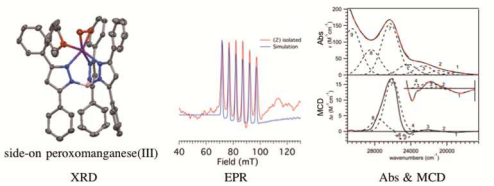

A peroxomanganese(III) species supported by a scorpionate (Tp) ligand has been characterized by X-ray crystallography, electron paramagnetic resonance and magnetic circular dichroism spectroscopy, revealing a distinct electronic structure.

Dalton Transactions Accepted Manuscript